Research Article

Understanding the Slow Motion of the Wangjiashan Landslide in the Baihetan Reservoir Area (China) from Space-Borne Radar Observations

Mingtang Wu,[1] Xiaoyu Yi ,[2] Jiawei Dun,[2] Jianyuan Yang,[1] Wei Cai,[1] and Guoqiang Zhang[2]

[1]*Zhejiang Huadong Construction Engineering CO. LTD, Hangzhou 310014, China*
[2]*State Key Laboratory of Geohazard Prevention and Geoenvironment Protection, Chengdu University of Technology, Chengdu 610059, China*

Correspondence should be addressed to Xiaoyu Yi; xiaou@stu.cdut.edu.cn

The analysis of landslide evolution using archived optical remote-sensing images is common, but it is often limited by the acquisition frequency, cloud cover, and resolution. With the development of space-borne radar observation technology, small baseline subset interferometric synthetic aperture radar (SAR) technology provides a new technical approach for detecting landslide deformation before disasters. The Sentinel-1A SAR datasets (20170219–20210330) were used to study the time-series deformation characteristics of the Wangjiashan landslide in the Baihetan Reservoir area before its impoundment. The time-series results show that the Wangjiashan landslide was in an initial deformation state in the prior four years, and the deformation first occurred in the middle part and then expanded to the landslide toe and crown retrogressive movement characteristics. Combined with an analysis of field deformation signs, these findings suggest that the upper landslide mass formed a local sliding surface, which caused serious deformation of the road. An analysis of historical rainfall data revealed that the Wangjiashan landslide is sensitive to rainfall, and the deformation is not only significantly correlated with cumulative rainfall but also influenced by concentrated heavy rainfall. The research in this study provides a basis for the monitoring, early warning, and risk management of the Wangjiashan landslide during the impoundment period. This work also provides a useful reference for investigations using space-borne SAR Earth observations in geological disaster prevention and control.

1. Introduction

The experience from the construction and impoundment of many large hydropower plants has shown that reservoir impoundment induces a large number of nascent landslide hazards while leading to increasing deformation of ancient landslides, resulting in many casualties and property losses [1–4]. Therefore, it is particularly important to understand the historical deformation of ancient landslides in reservoir inundation areas and then evaluate their stability. Due to the lack of monitoring equipment, the analyses of the deformation of landslides have mainly been performed using archived optical remote-sensing images [5, 6]. Optical remote sensing is characterized by wide coverage and a large spectral range but a long acquisition time interval; moreover, the images are affected by clouds and fog, and the spatial resolution is inadequate.

In recent years, with the development of Earth observation technology, interferometric synthetic aperture radar (InSAR) technology has provided a new technical way to study the historical deformation of landslides. The InSAR technique uses two or more synthetic aperture radar (SAR) images from the same area and the same orbit to perform interferometric differential processing to remove residual terrain errors, atmospheric effects, and other related errors to obtain high-precision three-dimensional information on the terrain and surface deformations. Compared with traditional ground measurement technology and space-borne optical remote sensing, InSAR technology has the characteristics of less weather influence, large-scare coverage, and

high measurement accuracy. It has played an important role in landslide deformation monitoring [7–14] and large-scale landslide detection [15–18]. With the continuous improvement of hardware and software of space-borne radar Earth observation technology, InSAR technology will play an even more important role in the future [19–22]. However, due to the variability of signal propagation and scattering characteristics, the measurement results of conventional differential InSAR (DInSAR) methods are mainly affected by systematic and random errors, i.e., satellite orbit errors, atmospheric delays, elevation errors, and surface scatterer variations. These may lead to temporal and spatial discorrelation and reduce the deformation monitoring accuracy [23–25]. In addition, these phenomena may also lead to the inability to extract surface deformation information in low-coherence regions. In contrast, the time-series InSAR technique can well compensate for the shortcomings of the traditional DInSAR technique, i.e., it uses a certain error reduction method to process multiple SAR images of long time series and then extracts the surface deformation information with high accuracy. Among the many time-series InSAR methods, the small baseline subset-InSAR (SBAS-InSAR) method has the advantage of obtaining small deformation information and long time series of slow surface deformation [18, 26, 27] and is therefore the most widely used in landslide monitoring.

Based on the above background, the SBAS-InSAR method is used to obtain the deformation rates of the Wangjiashan ancient landslide in the radar line-of-sight (LOS) and slope aspect directions based on Sentinel-1A radar images and to extract historical time-series deformation information of this landslide. Furthermore, the landslide deformation characteristics and influencing factors are analyzed in conjunction with a field investigation. On this basis, the evolution trend of the Wangjiashan landslide in the impoundment period is discussed. The research in this study provides a basis for the monitoring, early warning, and risk management of the Wangjiashan landslide during the impoundment period. This work also provides a useful reference for investigations using space-borne SAR Earth observations in geological disaster prevention and control.

2. Wangjiashan Landslide

Due to increasing demands for clean energy and the unique geographical conditions of Southwest China, several hydropower stations, including the Baihetan Hydropower Station, have been built in the lower reaches of the Jinsha River in this region. Within the Baihetan Reservoir area is the Wangjiashan landslide, which is located on the right bank of the Xiaojiang River and is only 1.3 km from the Xiangbiling resettlement area (Figure 1). This valley is characterized by a subtropical dry and warm climate with an average annual temperature ranging from 12 C to 20 C. The annual precipitation in the study area is approximately 600–800 mm, with precipitation falling more frequently from May to October, and this period accounts for 90% of the annual rainfall; in contrast, from November to April of the following year, the weather is sunny and dry with sparse rainfall.

The Wangjiashan landslide is 800 m long and 90–500 m wide and covers approximately $23.5 \times 10^4 \, m^2$ (Figure 2). The elevation of the landslide toe on the right bank of the Xiaojiang River is approximately 765 m, while the crown is at an elevation of 1125 m, resulting in an elevation difference of 360 m between the landslide crown and toe. Gullies bound the left and right sides of the landslide, and these two gullies extended upward, ultimately intersecting at the landslide crown. The 870–950 m elevation section of the landslide features flat-topped hills and landslide depressions, and the terrain slope is 15–20°, whereas from an elevation of 870 m to the toe of the landslide, the terrain slope is 35–40°, and the local slope ranges from 45–50°.

The longitudinal profile of the landslide taken from the borehole data (see Figure 2, for borehole location) of the Power China Huadong Engineering Corporation (EHEC) is shown in Figure 3. The deposits on the upper landslide are mainly gravel soil that is gray-yellow, loose, and 14.0–49.9 m thick, whereas the lower landslide deposits are silty gravel that is also gray-yellow to dark gray in color, dense, and 3.04–13.30 m thick. The soil in the sliding zone comprises gray-black to gray-brown gravel clay distributed in interlayers with silty gravel in the lower part of the landslide. The landslide bed is bedrock composed of Ordovician, Devonian, and Carboniferous limestone, dolomite, and quartz sandstone intercalated with siltstone, mudstone, and shale. The strata are oriented N0-10 W and dip NE∠40–46°, and the strata are affected by the tectonic effect; moreover, the joint network is dense, and the rock mass is broken and highly weathered. According to drilling data, the landslide deposit is 14.0–87.6 m thick, with a total volume of approximately $611 \times 10^4 \, m^3$. The landslide has long exhibited creep deformation, and thus, the stability and disaster risk of the Wangjiashan landslide after the impoundment of the Baihetan Reservoir has aroused concern among hydropower station authorities. Now, it is urgent to understand the deformation characteristics of the Wangjiashan landslide before impoundment to reduce or eliminate the risk of geological disasters during impoundment.

3. Data and Methods

3.1. Data. Because the ancient Wangjiashan landslide tends to move toward the SW, the terrain slope is smaller than the complementary angle of the central incident angle (36.8°) of the Sentinel-1A descending track [28]. Hence, Sentinel-1A descending track data are conducive to analyzing the deformation the landslide. The coverage of the Sentinel-1A descending track data is shown in Figure 1. In this study, 77 scenes from the descending track of Sentinel-1A are used to investigate the historical deformation of the Wangjiashan landslide before impoundment from February 19, 2017, to March 30, 2021, with a time interval of 12 days. To eliminate the influence of terrain relief on the InSAR results, the Advanced Land Observing Satellite (ALOS) World 3D (AW3D30) digital elevation model (DEM) with a spatial resolution of 12.5 m is used as the external DEM data to simulate the terrain phase.
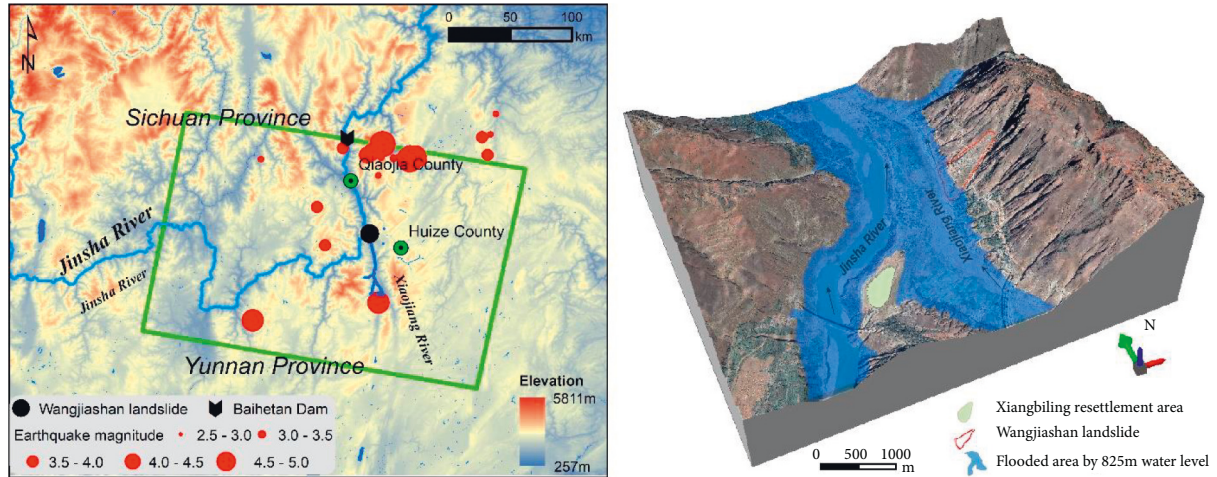
FIGURE 1: The location of the Baihetan Dam and Wangjiashan landslide, and the coverage of Sentinel-1A descending track data is superimposed in the green polygon. In addition, the epicenter and magnitude of earthquakes within 100 km of the Wangjiashan landslide from 2017 to 2020 are marked.

Moreover, to reduce the phase error caused by the orbit error, before processing the Sentinel-1A data, we download precise orbit data at the corresponding time and import the relevant data to correct the orbit information. In addition, monthly precipitation data and seismic data for the study area from January 2017 to March 2021 are acquired from the China Meteorological Data Service Center and the China Earthquake Networks Center, respectively. Finally, the engineering geological information of the Wangjiashan landslide is obtained from the geotechnical investigation report of the EHEC.

3.2. SBAS-InSAR Method.

The SBAS-InSAR approach was first proposed by Italian scholars Berardino et al. [29]. SBAS-InSAR technology overcomes the decoherence phenomenon caused by an excessively long spatiotemporal baseline and alleviates atmospheric effects and terrain influences on the interferometric difference [29, 30]. The SBAS-InSAR technique obtains time series of surface deformation by the least-squares method while using singular value decomposition (SVD) to fit the deformation in both time and space; the InSAR surface deformation monitoring accuracy reaches the millimeter level, and thus, this technique exhibits a high measurement accuracy in landslide deformation monitoring research [31].

$N + 1$ scenes of SAR images are acquired in the same area and arranged in chronological order; then, one scene is chosen as the main image for registration, while the other SAR images are registered to the main image by setting appropriate temporal and spatial baseline thresholds. Ultimately, M scene interferograms are obtained. Assuming that t is the image acquisition time, after removing the flat terrain effect, terrain phase, and atmospheric phase error, the interference phase $\delta_\varphi(x, r)$ at pixel point (x, r) (x is the azimuth coordinate and r is the range coordinate) can be obtained from the phases $\varphi(t_A, x, r)$ and $\varphi(t_B, x, r)$ in the images generated at times t_A and t_B, respectively [29, 32, 33].

During SBAS-InSAR data processing, M interferograms are generated. $\varphi(x, r)$ is adopted to represent the matrix composed of the image deformation phases at point (x, r) at N times; then, the matrix composed of M interferometric pair phase values is $\delta_\varphi(t_A, x, r) = \mathbf{A}\varphi(x, r)$, where A is an $M \times N$ matrix. When $M \geq N$, the deformation time series can be obtained by the least-squares method. When $M < N$, the result obtained by the least-squares method is not unique, SVD is implemented to jointly solve multiple small baselines, and the phase velocities obtained for each period are integrated into the time domain to obtain the deformation time series of the entire observation period.

In this study, ENVI SARscape software is used to analyze the historical deformation of the Wangjiashan landslide. The temporal baseline threshold is set to 72 days, and the critical baseline percentage is 2%. The 20201025 SAR image is used as the main image, while images from other periods are used as auxiliary images for interferometric pairing, and 213 sets of interferometric pairs are generated. The relationship between the specific acquisition dates of the descending track data and the spatiotemporal baseline is shown in Figure 4. Synthetic interferogram inversion, geocoding, and raster vector conversion are performed to generate the mean LOS deformation rate, and finally, the time-series deformation results are obtained.

3.3. Slope Aspect Velocity Fields.

The sliding direction of a landslide is generally downward along the slope. In the process of radar interferometry, the obtained deformation is usually the deformation value along the radar LOS direction, which often cannot accurately reflect the true deformation of the slope surface [34, 35]. According to the geometric relationship among the radar LOS direction, the slope aspect, and the vertical settlement direction, the deformation in the radar LOS direction (V_{LOS}) is transformed into slope aspect deformation (V_{Slope}) [36, 37]. The specific conversion formula is as follows:
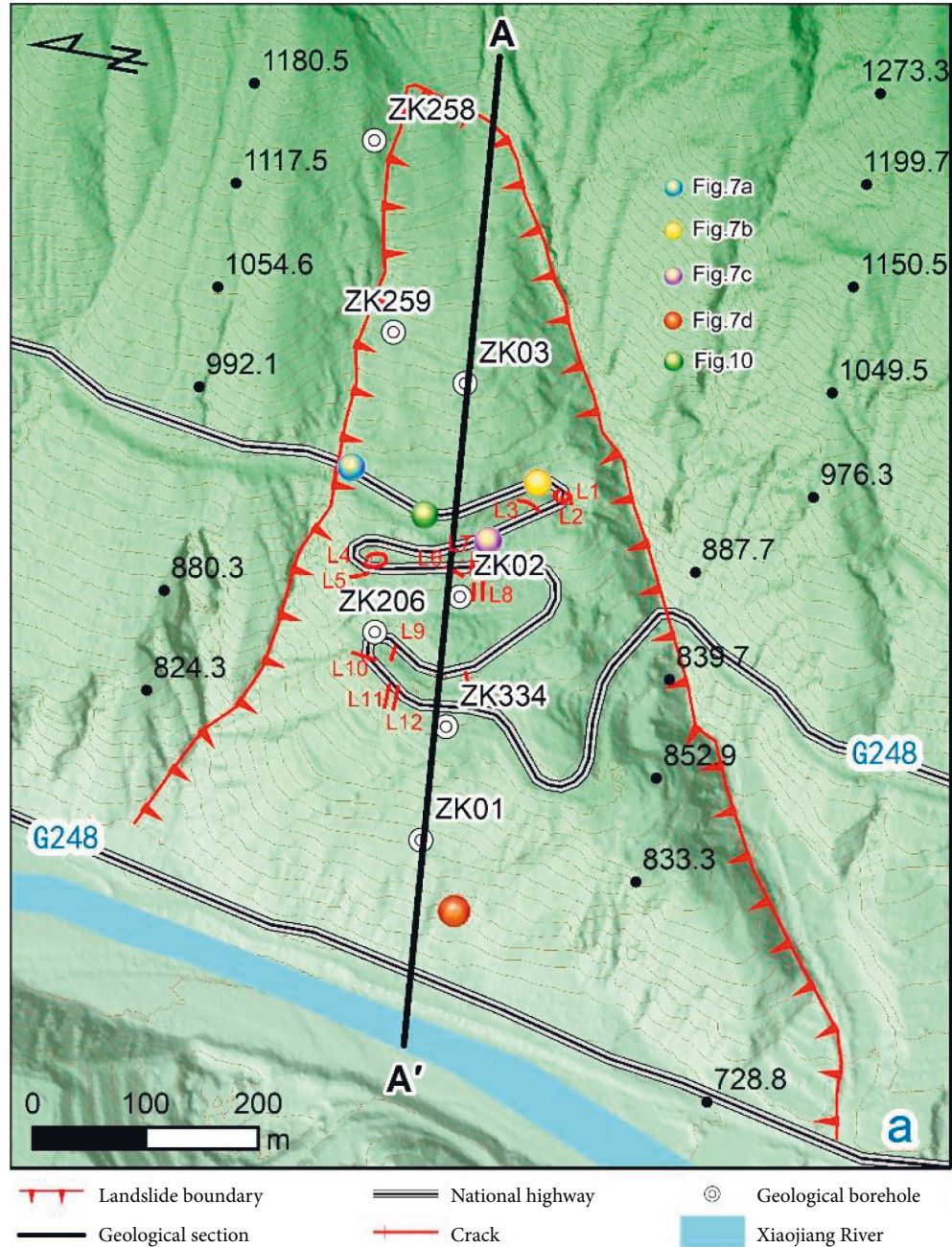
FIGURE 2: Geological map of the Wangjiashan landslide.

$$V_{\text{Slope}} = \frac{V_{LOS}}{\text{Index}}, \tag{1}$$

$$\text{Index} = n_{LOS} \times n_{\text{Slope}}, \tag{2}$$

$$n_{LOS} = (-\sin \theta \cos \theta, \ \sin \theta \sin \alpha, \ \cos \theta), \tag{3}$$

$$n_{\text{Slope}} = (-\sin \beta \cos \varphi, -\cos \beta \sin \varphi, \ \sin \varphi). \tag{4}$$

In the above equations, θ represents the incident angle of the radar, α is the satellite flight direction angle, β is the slope direction, and φ is the slope. Among them, β and φ can be calculated from the DEM.

(1) demonstrates that if the value of Index is close to 0, V_{Slope} will tend toward infinity, but the ground unit at this time is completely decoherent. To correct this anomaly, according to the study of Herrera et al. [38], |Index| = 0.3 can be set as a threshold so that the acceptable projected velocity value can be distinguished from the data with unreliable projection values. That is, when −0.3 < Index < 0, Index = −0.3, and when 0 < Index < 0.3, Index = 0.3. In addition, when $V_{\text{Slope}} > 0$, the landslide mass moves upward along the slope. Even if expansion causes a bulge on the front edge of the landslide or the landslide mass accumulates at the foot of the slope, the displacement vector in the horizontal direction remains oriented in the downward direction of the
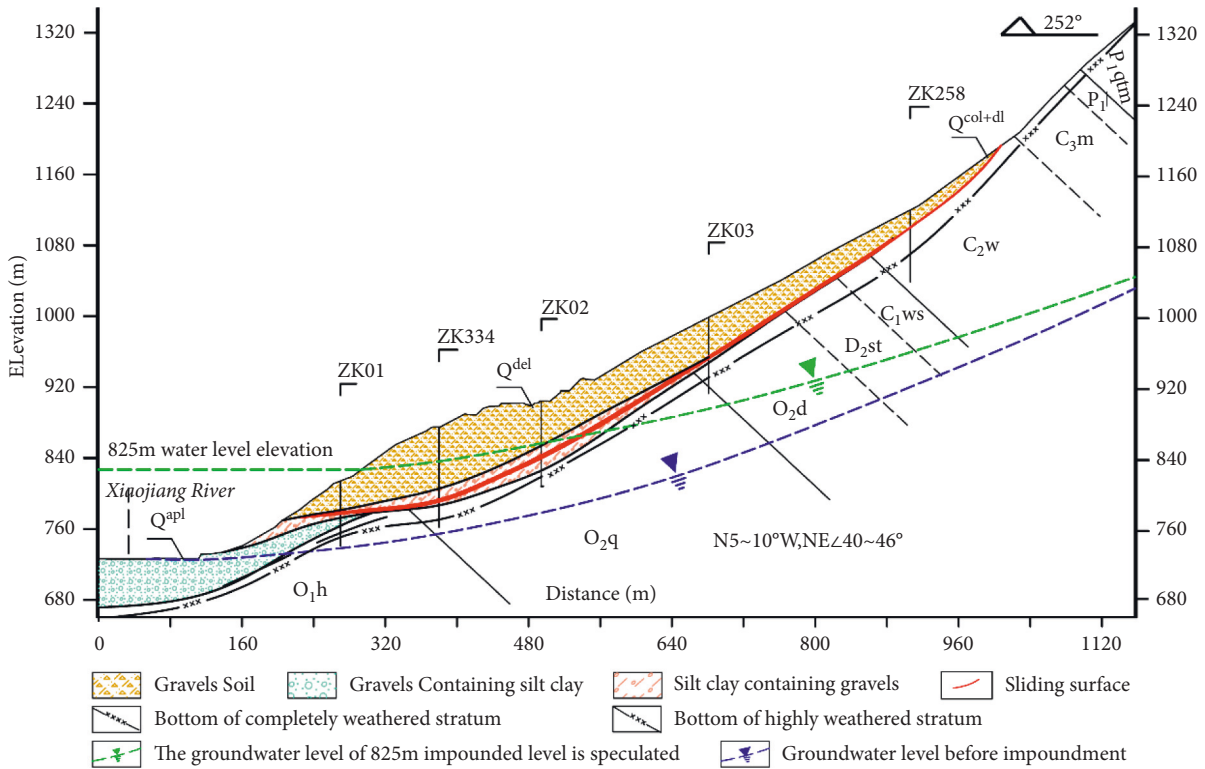
FIGURE 3: Longitudinal profile A-A$'$ of the Wangjiashan landslide in Figure 6.
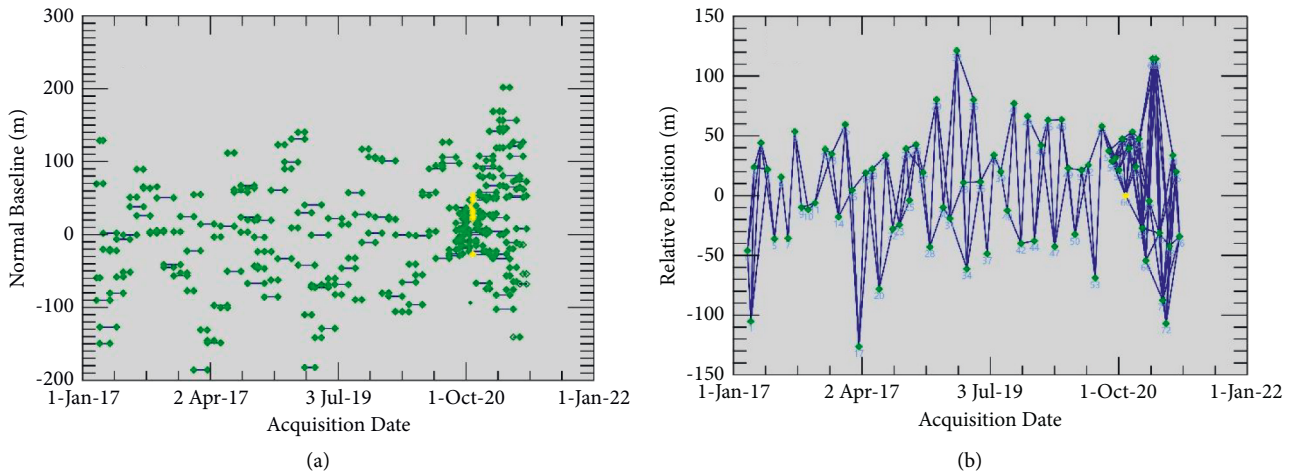

(a)

(b)

FIGURE 4: Spatial and temporal baselines of SAR datasets used in this study: (a) time-baseline plot of interferometric pairs of SAR images; (b) time-position plot of SAR image.
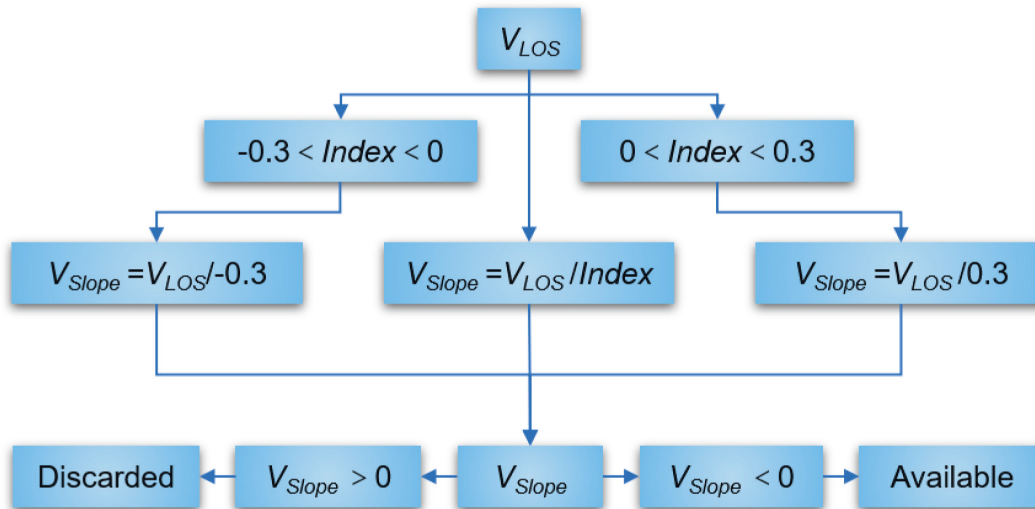
FIGURE 5: Flowchart of calculating slope aspect velocity fields from LOS direction velocity fields.

V_{LOS} (mm/year)
- -69 - -55
- -55 - -41
- -41 - -27
- -27 - -13
- -13 - 0
- 0 - 14

V_{Slope} (mm/year)
- -220 - -200
- -220 - -160
- -160 - -120
- -120 - -80
- -80 - -40
- -40 - 0

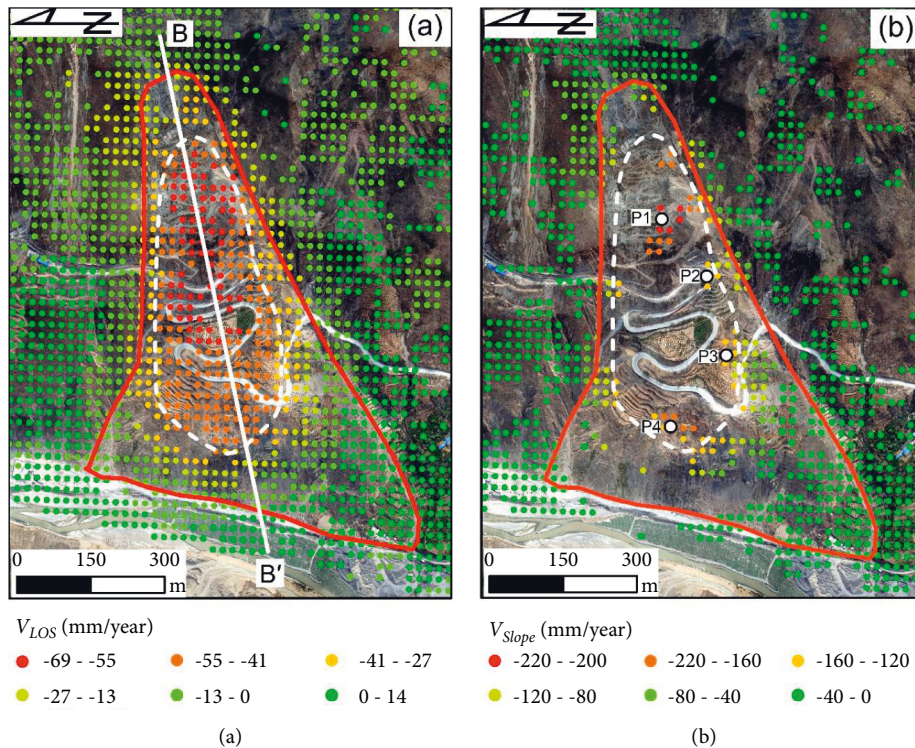(a)   (b)

FIGURE 6: The mean deformation velocity of the Wangjiashan landslide (201702–202103): (a) LOS directional deformation rate; (b) slope aspect deformation rate.

slope surface. These deformation points with $V_{Slope} > 0$ need to be eliminated consistently. In this way, the average deformation rate of the surface displacement along the slope direction in the study area can be obtained (Figure 5).

4. Results

4.1. Mean Deformation Velocities. In this study, the SBAS-InSAR method is utilized to analyze the mean deformation rate of the Wangjiashan landslide in the radar LOS and slope aspect directions. As shown in Figure 6, the mean deformation rate of the Wangjiashan landslide in the LOS direction ranges from −69 to −14 mm/year, while the mean deformation rate in the slope aspect direction reaches −220 mm/year. The landslide deformation is concentrated in the white dashed circle in the middle with a longitudinal length of approximately 600-700 m. The mean V_{LOS} ranges from −41 to −69 mm/year, and the mean V_{Slope} ranges from
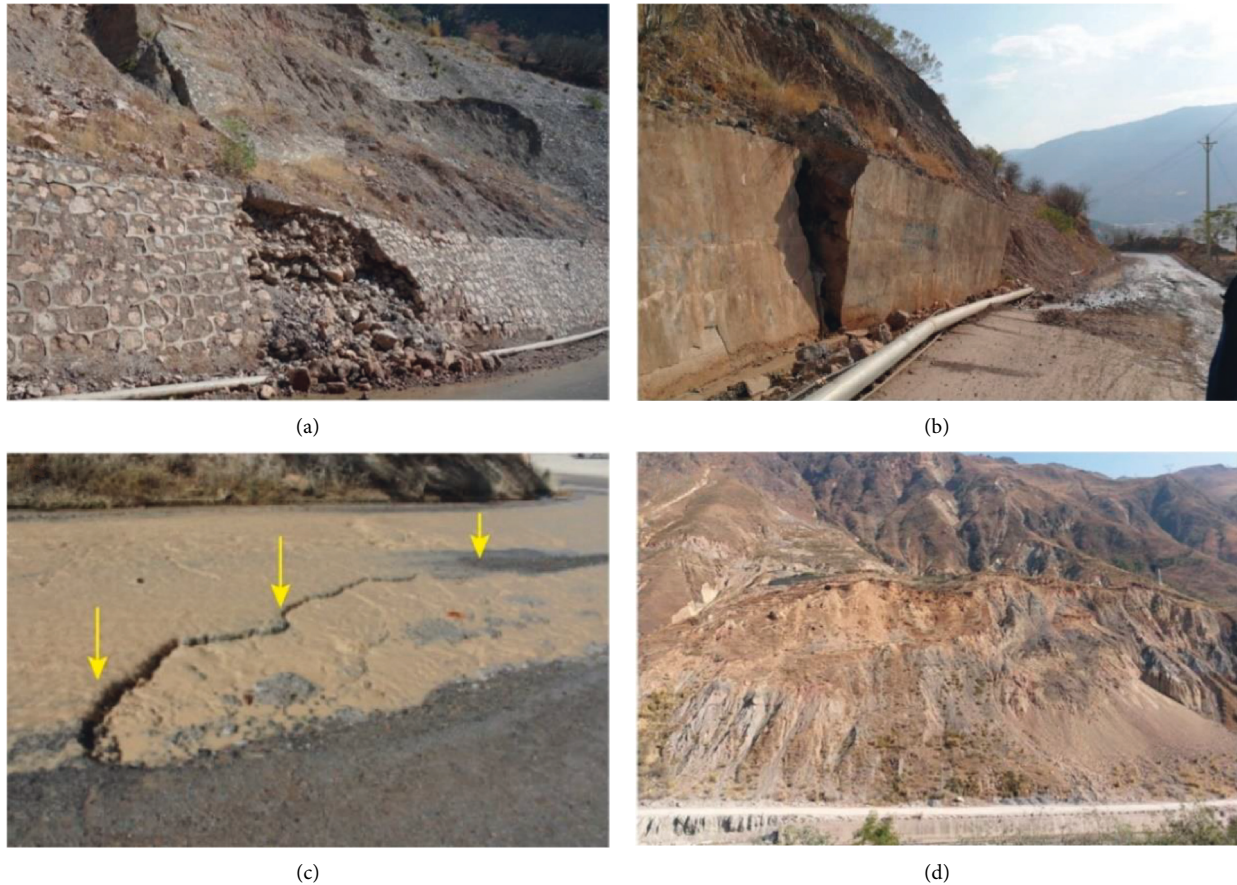
(a)

(b)

(c)

(d)

FIGURE 7: Photographs of deformation signs of Wangjiashan landslide: (a) broken retaining wall; (b) toppling of retaining wall; (c) tension cracks in road surface; (d) landslide deformation on the front edge of the landslide.

−120 to −220 mm/year. The field investigation revealed deformation phenomena such as fracturing (Figure 7(a)) and toppling of the retaining wall (Figure 7(b)) in the area of the white dashed circle. Furthermore, as many as 12 cracks are found in the slope (Figure 2); the longest crack is approximately 17 m long, and the tensile crack with the maximum width is 30 cm wide (Figure 7(c)). These cracks are mostly located around the road and are dominated by tension cracks, which may be the result of landslide deformation caused by road excavation. Some deformation phenomena, such as local collapse in front of the landslide, are also observed (Figure 7(d)).

4.2. Time-Series Cumulative Deformation.
Based on SBAS-InSAR technology, nine time-series cumulative deformation graphs of the Wangjiashan landslide are obtained (Figure 8). It should be noted that all accumulated deformation is referenced to the first image on February 19, 2017. In 2018, the deformation area of the landslide was in the middle of the landslide area (red part). In 2019, the landslide deformation expanded to the front and rear edges. Over time, the deformation of the Wangjiashan landslide gradually increased, and the maximum cumulative deformation in the LOS direction reached 294 mm. As shown in Figure 9, the deformation of the Wangjiashan landslide exhibits obvious

spatial heterogeneity, with the largest deformation in the middle of the landslide, followed by the landslide toe, and the smallest deformation at the landslide crown. According to the field investigation, the cracks are mainly developed in the middle of the landslide (Figure 2 and Table 1), consistent with the area with the largest cumulative deformation.

5. Interpretation of Landslide Motion

5.1. Kinematic Behavior.
To further understand and analyze the temporal and spatial characteristics of landslide deformation, the mean LOS deformation rate curve along section B–B′ in Figure 6(a) and the LOS cumulative deformation curve along section B–B′ in Figure 9 are superimposed onto the geological profile, and the result is shown in Figure 5. A comparison of the data revealed the following:

(i) The largest deformation of the Wangjiashan landslide is in zones B and C. The average LOS cumulative deformation is 220 mm, and the maximum LOS cumulative deformation is 289 mm. The deformation of area A is relatively low; the average LOS cumulative deformation in zone A is 90 mm, and the maximum LOS cumulative deformation is 120 mm. Likewise, the deformation in area E is very weak; the average LOS deformation rate is only eight mm/year.
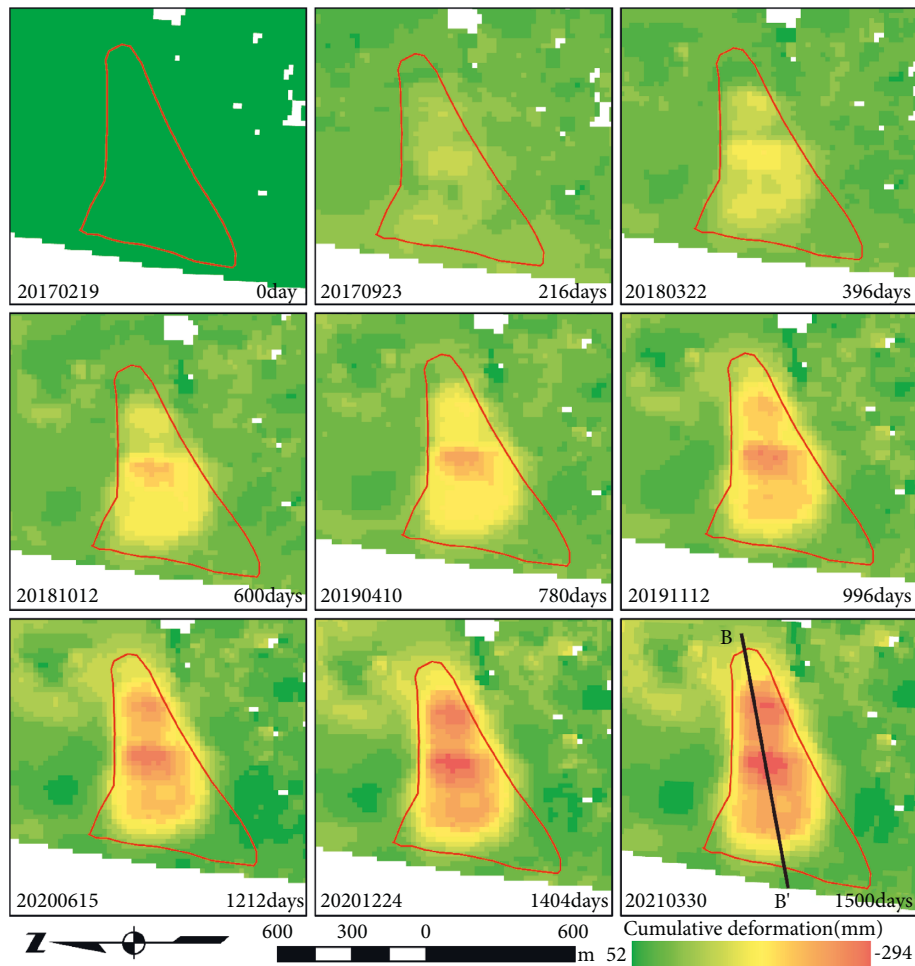
FIGURE 8: The time-series cumulative deformation maps along the LOS from February 19, 2017, to March 30, 2021, with a reference SAR acquisition date of 20170219.

The cumulative deformation and LOS deformation rate in zone *D* increase along the profile. The deformation rate at the crown of the Wangjiashan landslide is the smallest, while the deformation rates of the central zone (zone C) and the toe (zone B) are larger. As shown in Figure 5, the middle of the landslide deformed first and then expanded to the front and rear edges. The landslide exhibits the deformation characteristics of a retrogressive landslide [39].

(ii) The data of zone F show a decreasing deformation rate but increasing cumulative deformation. A field investigation revealed that the retaining wall on the side of the road in this area is broken (Figure 7(b)), and the road surface was bulging (Figure 10) and cracked (Figure 7(c)). These observations indicate that the sliding force of the landslide mass exceeded the slip resistance of the retaining wall, resulting in damage to both the retaining wall and the ground. Considering the deformation rate in conjunction with the topographic characteristics [40, 41], due to excavation of the road, the upper landslide seems to have formed a local sliding surface, leading to serious road deformation. Of course, the final determination of this local sliding surface requires further detailed research.

5.2. Influencing Factors and Evolution Trend.
Gravity-driven retrogressive sliding is the main deformation mechanism of the Wangjiashan landslide. However, other factors, such as changes in the groundwater level, heavy rainfall, and earthquakes, can accelerate deformation [42]. Nevertheless, no groundwater was discovered in the boreholes in the Wangjiashan landslide, which indicates that the groundwater level within the landslide is much lower than the sliding surface (Figure 3). Therefore, groundwater is not the main factor affecting landslide deformation. To understand the response relationship between deformation and rainfall, four monitoring points (P1, P2, P3, and P4 in Figure 6(b)) with different elevations are selected from the slope deformation rate map to further analyze the correlation between the slope time-series deformation and the precipitation observed by adjacent meteorological stations.
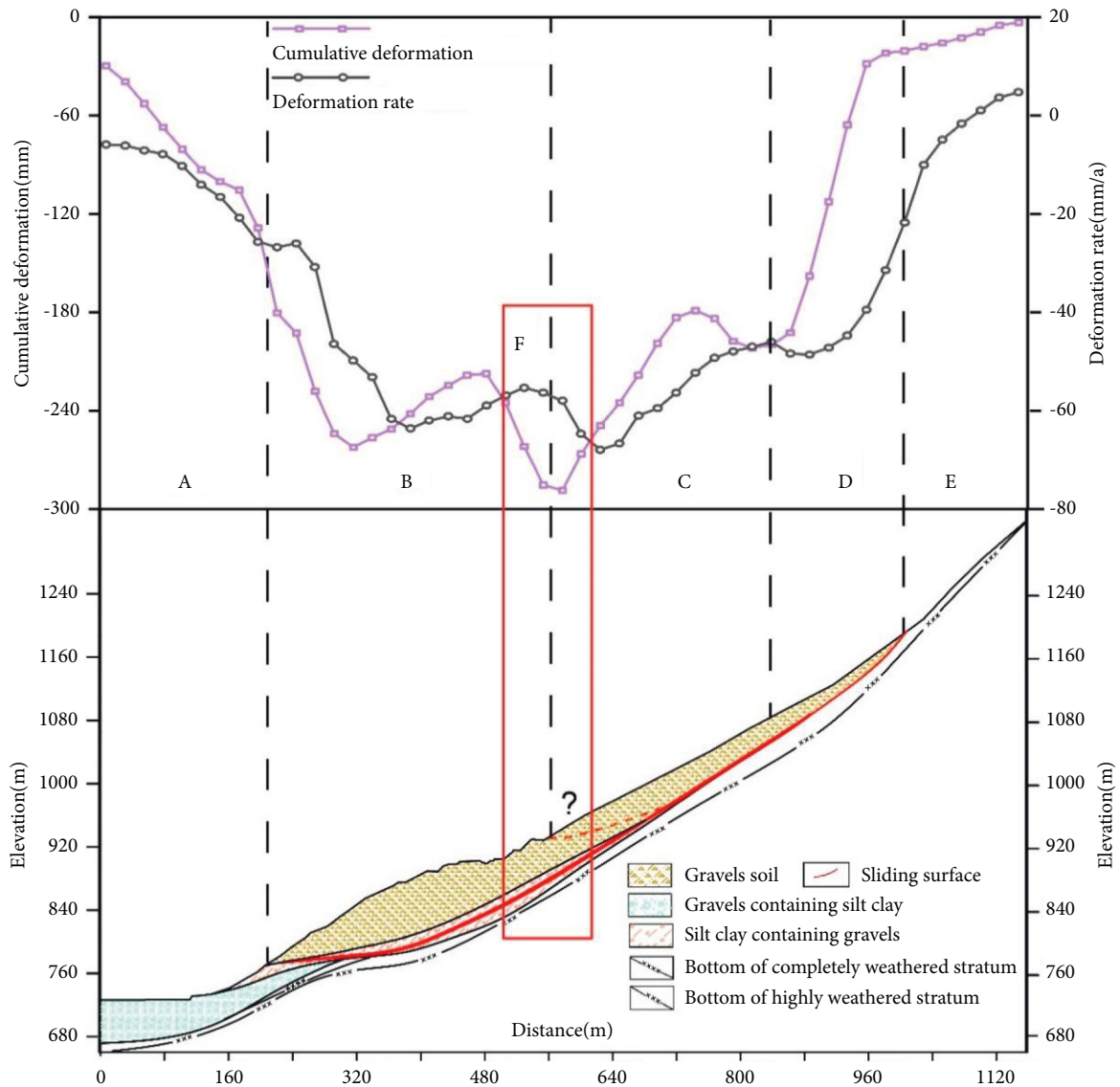
FIGURE 9: Landslide LOS deformation rate curve and cumulative deformation curve along profile B–B′ calculated by the SBAS-InSAR technique.

TABLE 1: Characteristics of tensile cracks in Figure 2.

Crack number	Altitude (m)	Strike angle (°)	Extension length (m)	Width (cm)
L1	945	EW	10	20–30
L2	945	N20°W	17	1–2
L3	943	N60°E	7	3–5
L4	914	EW	10	5–10
L5	912	N20°E	12	0.5–1
L6	916	N20°W	10	1–2
L7	898	N60°E	10	0.5–1
L8	887	N66°E	10	1–10
L9	885	N85°E	10	1–5
L10	880	EW	8	2–5
L11	879	N10°W	15	5–15
L12	874	EW	9	2–3

Figure 10: Cracks in the retaining wall and bulging deformation of the road.
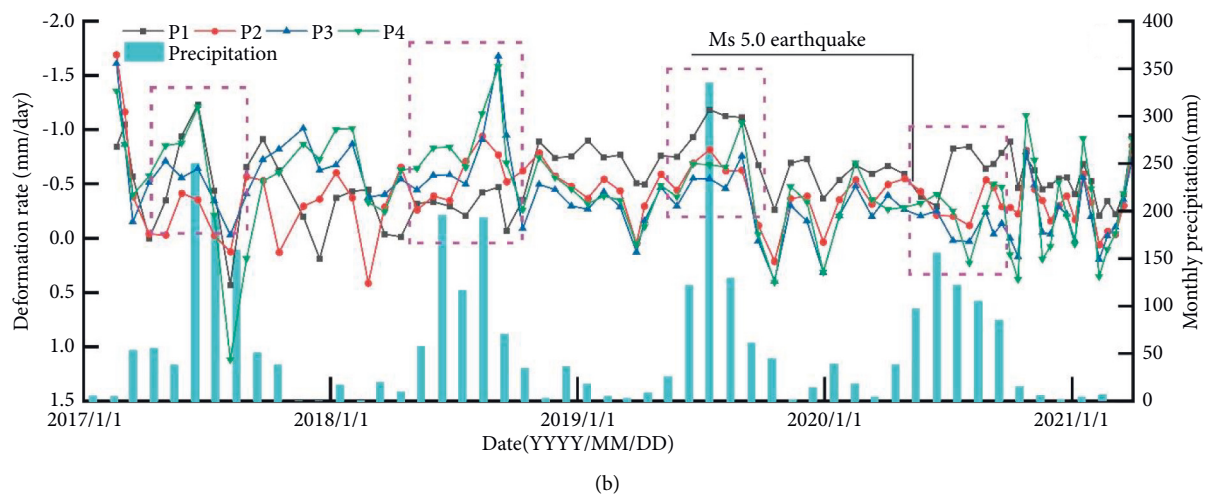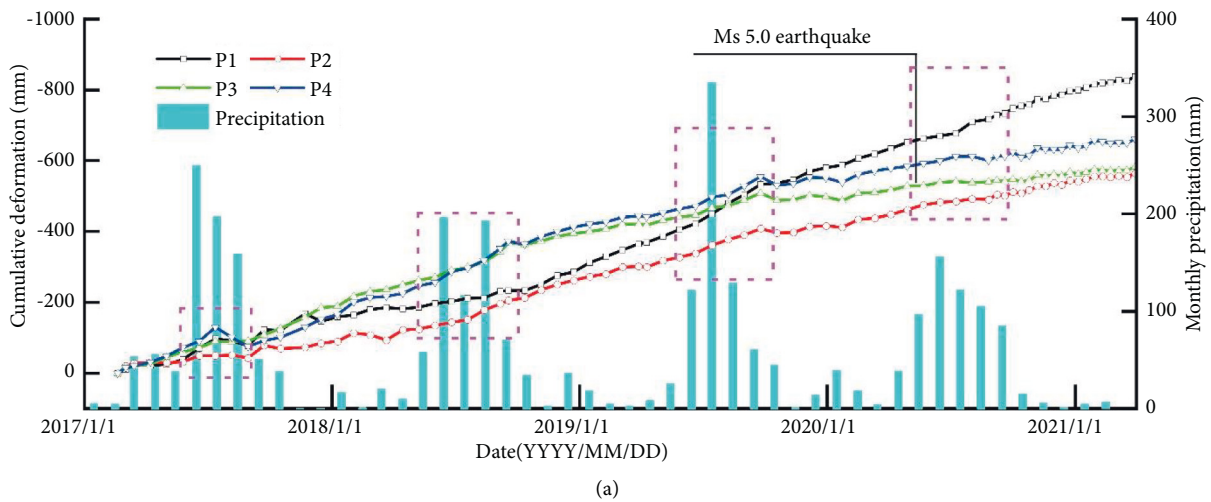

(a)

(b)

Figure 11: Correlation between the Wangjiashan landslide slope aspect deformation and rainfall. P1, P2, P3, and P4 are located at different elevations of the Wangjiashan landslide (Figure 6(b)): (a) cumulative deformation; (b) deformation rate.
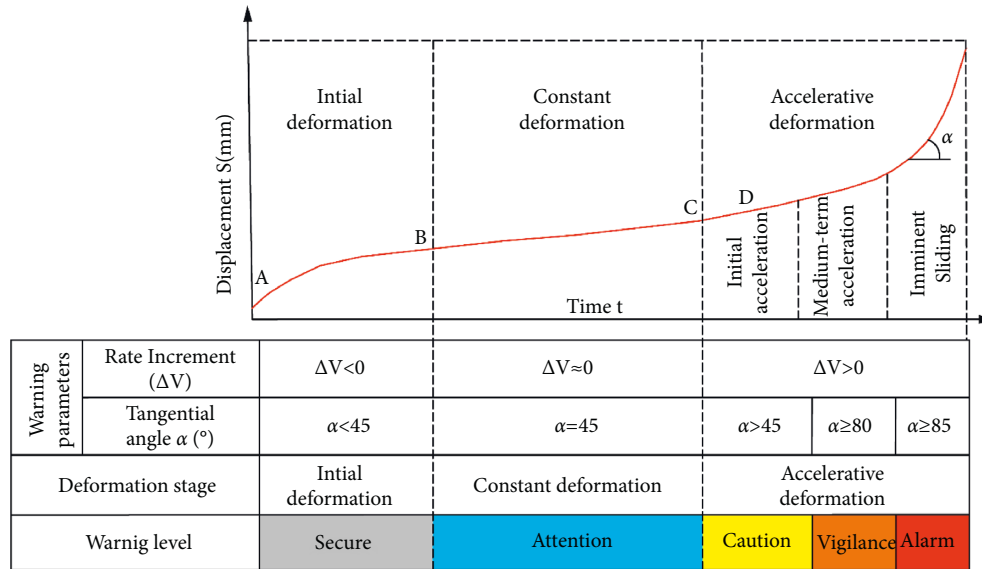
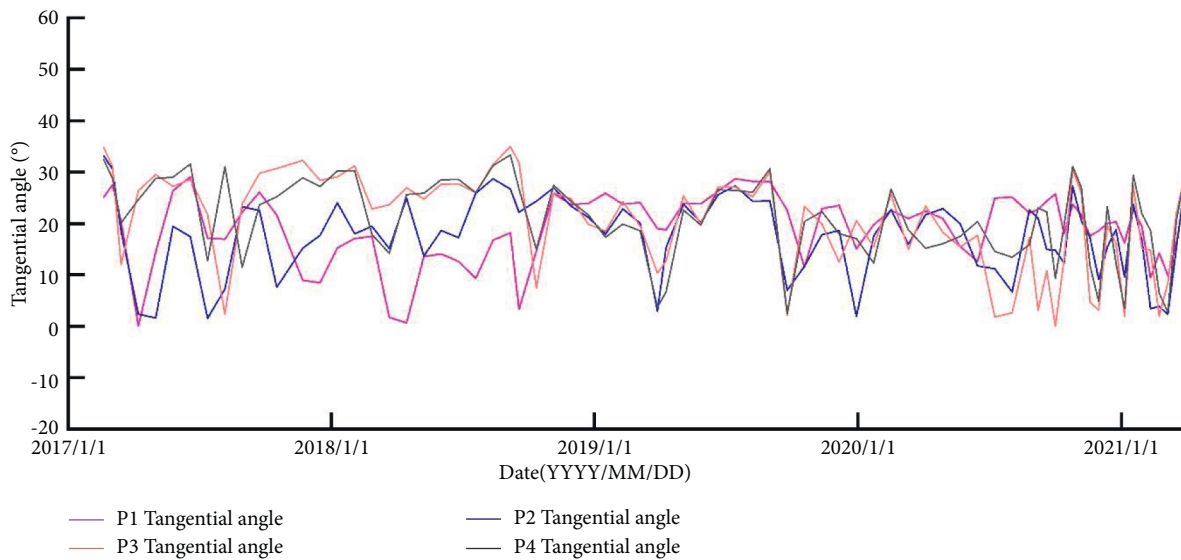FIGURE 12: Eary warning criteria for creep failure of a slope [46].

P1 Tangential angle
P2 Tangential angle
P3 Tangential angle
P4 Tangential angle

FIGURE 13: Time history of tangential angle α of P1~P4 in Figure 11.

Figure 11 shows the slope aspect time-series cumulative deformation and deformation rate of the Sentinel-1A data from February 2017 to March 2021 at the four observation points P1, P2, P3, and P4. The deformations at P1, P2, P3, and P4 increase linearly, and the deformations increase obviously during the rainy season. In the rainy season of 2017, the deformations at the four observation points increased. However, in the 2018 rainy season, only the deformations at P2, P3, and P4 changed significantly with seasonal precipitation. In July 2019, the monthly precipitation reached 334.5 mm, and the cumulative displacements at the four observation points increased significantly. Through the deformation rate curve of the landslide time series, we can see that the displacement rate of landslides in the rainy season is increased compared with that in the dry season. This shows that heavy rainfall will accelerate the

deformation of a landslide. Because the Wangjiashan landslide is a reactivated ancient landslide, there is also deformation in the dry season, but the deformation rate is less than that in the rainy season. These findings indicate that rainfall is one of the main reasons for the reactivation and deformation of the Wangjiashan landslide.

In contrast, during the rainy season of 2020, the deformations at the four observation points did not increase significantly because the rainfall was low. In addition, the cumulative rainfall from June to August in the study area during 2019 and 2018 was 504.5 mm and 584.5 mm, respectively, and the cumulative deformation at point P2 was 61.86 mm and 50.38 mm, respectively. The above phenomenon indicates that concentrated heavy rainfall is more likely to cause large deformation of the landslide [43, 44]. The above data analysis shows that the

deformation of the Wangjiashan landslide in the rainy season is related to the accumulation of rainfall and concentrated heavy rainfall.

In addition, seismic data within a 100 km radius of the Wangjiashan landslide from 2017 to 2020 were downloaded from the China Earthquake Networks Center (http://www.ceic.ac.cn/) (Figure 2). Based on its epicentral location, focal depth, magnitude, and intensity, the Ms5.0 earthquake at 21 : 47 on May 18, 2020, caused many houses to collapse and damaged several roads in Qiaojia County. The epicenter of the earthquake was 74 km from the Wangjiashan landslide, and the focal depth was 8 km. However, comparative data show that the earthquake did not accelerate the deformation of the Wangjiashan landslide (Figure 11).

6. Discussion

According to the theory of creep deformation [45], before a landslide occurs, it usually undergoes an initial deformation stage, a constant deformation stage, and an accelerated deformation stage (which in turn is divided into three substages: an initial acceleration stage, a moderate acceleration stage, and an imminent sliding stage). As shown in Figure 12, Xu et al. [47, 48] proposed using the tangential angle (α) as the basis for dividing these three stages. When the tangent angle is much less than 45°, the landslide is considered to be in its initial deformation stage; when the tangent angle is approximately equal to 45°, the landslide is assumed to undergo constant velocity deformation; when the tangent angle greatly exceeds 45°, the landslide is believed to be in its accelerated deformation stage (with 80° and 85° representing the boundaries between the first and second substages and the second and third substages, respectively). The gravity landslide warning model shown in Figure 12 has been widely used to monitor and warn landslides in Northwest and Southwest China [46, 49–53].

The long-term displacement curve in Figure 11 shows that the Wangjiashan landslide has exhibited a stable deformation rate in the past four years, except for a briefly accelerated rate during the rainfall period and average tangential angle α between 23° and 32°, which is less than 45° (Figure 13). Therefore, from the perspective of its evolution, the Wangjiashan landslide was in the initial deformation stage before impoundment and maintained slow deformation without strong interference from external factors.

The signs of deformation during the impoundment period of the Wangjiashan landslide and studies on areas such as the Three Gorges Reservoir have shown that fluctuations in the water level of large reservoirs may lead to the reactivation of ancient landslides, resulting in considerable losses [3, 4, 54, 55]. Given the rainfall concentration characteristics of the study area and the sensitivity of the deformation of the Wangjiashan landslide to rainfall, its future development deserves further attention. Therefore, it is urgent to systematically identify and analyze potential landslides in the Baihetan Reservoir area and establish a monitoring and early warning system to reduce the losses of life and property.

7. Conclusions

Sentinel-1A SAR data were used to study the time-series deformation characteristics of the Wangjiashan landslide in the Baihetan Reservoir area before its impoundment. We found that the Wangjiashan landslide has been in an initial deformation state in recent years. Deformation first occurred in the middle of the landslide and then expanded to the landslide toe and crown, thereby demonstrating the characteristics of retrogressive movement. Combined with an analysis of field deformation evidence, the upper landslide mass seems to have formed a local sliding surface, which has caused serious deformation of the road. An analysis of historical rainfall data revealed that the Wangjiashan landslide is sensitive to rainfall, and the deformation is not only significantly correlated with cumulative rainfall but also influenced by concentrated heavy rainfall. Considering the sensitivity of the Wangjiashan landslide to rainfall, coupled with the environmental changes caused by impoundment, establishing a landslide monitoring and early warning system in this area is particularly important.

Data Availability

The precipitation data and historical earthquake data were provided by China Meteorological Data Service Center (http://data.cma.cn/) and China Seismic Network Center (http://www.ceic.ac.cn/), respectively. Sentinel-1 A/B images were from the European Space Agency (ESA) project, and these data were downloaded from the Sentinel-1 Scientific Data Hub. DEM data were provided by the Japan Aerospace Exploration Agency (JAXA).

Conflicts of Interest

The authors declare that they have no conflicts of interest.

Acknowledgments

References

[1] D. Huang and D. M. Gu, "Influence of filling-drawdown cycles of the Three Gorges reservoir on deformation and failure behaviors of anaclinal rock slopes in the Wu Gorge," *Geomorphology*, vol. 295, pp. 489–506, 2017.

[2] B. Huang, Y. Yin, G. Liu, S. Wang, X. Chen, and Z. Huo, "Analysis of waves generated by Gongjiafang landslide in Wu Gorge, three Gorges reservoir, on November 23, 2008," *Landslides*, vol. 9, no. 3, pp. 395–405, 2012.

[3] H. Tang, J. Wasowski, and C. H. Juang, "Geohazards in the three Gorges reservoir area, China - lessons learned from decades of research," *Engineering Geology*, vol. 261, p. 105267, 2019.

[4] Y.-p. Yin, B. Huang, X. Chen, G. Liu, and S. Wang, "Numerical analysis on wave generated by the qianjiangping landslide in three Gorges reservoir, China," *Landslides*, vol. 12, no. 2, pp. 355–364, 2015.

[5] R. Behling, S. Roessner, D. Golovko, and B. Kleinschmit, "Derivation of long-term spatiotemporal landslide activity-A multi-sensor time series approach," *Remote Sensing of Environment*, vol. 186, pp. 88–104, 2016.

[6] C. Wu, X. Li, W. Chen, and X. Li, "A review of geological applications of high-spatial-resolution remote sensing data," *Journal of Circuits, Systems, and Computers*, vol. 29, no. 6, Article ID 2030006, 2020.

[7] P. Liu, Z. Li, T. Hoey et al., "Using advanced InSAR time series techniques to monitor landslide movements in Badong of the Three Gorges region, China," *International Journal of Applied Earth Observation and Geoinformation*, vol. 21, pp. 253–264, 2013.

[8] K. Dai, Z. Li, R. Tomás et al., "Monitoring activity at the Daguangbao mega-landslide (China) using Sentinel-1 TOPS time series interferometry," *Remote Sensing of Environment*, vol. 186, pp. 501–513, 2016.

[9] R. Tomás, Z. Li, J. M. Lopez-Sanchez, P. Liu, and A. Singleton, "Using wavelet tools to analyse seasonal variations from InSAR time-series data: a case study of the Huangtupo landslide," *Landslides*, vol. 13, no. 3, pp. 437–450, 2016.

[10] X. Hu, R. Bürgmann, W. H. Schulz, and E. J. Fielding, "Four-dimensional surface motions of the Slumgullion landslide and quantification of hydrometeorological forcing," *Nature Communications*, vol. 11, no. 1, 2020.

[11] I. N. S. Parwata, S. Nakashima, N. Shimizu, and T. Osawa, "Effect of digital elevation models on monitoring slope displacements in open-pit mine by differential interferometry synthetic aperture radar," *Journal of Rock Mechanics and Geotechnical Engineering*, vol. 12, no. 5, pp. 1001–1013, 2020.

[12] Q. Meng, W. Li, F. Raspini et al., "Time-series analysis of the evolution of large-scale loess landslides using InSAR and UAV photogrammetry techniques: a case study in Hongheyan, Gansu Province, Northwest China," *Landslides*, vol. 18, no. 1, pp. 251–265, 2021.

[13] C. Zhou, Y. Cao, K. Yin et al., "Landslide characterization applying sentinel-1 images and InSAR technique: the muyubao landslide in the three Gorges reservoir area, China," *Remote Sensing*, vol. 12, no. 20, p. 3385, 2020.

[14] C. Zhou, Y. Cao, X. Hu, K. Yin, Y. Wang, and F. Catani, "Enhanced dynamic landslide hazard mapping using MT-InSAR method in the Three Gorges Reservoir Area," *Landslides*, 2022.

[15] R. Guo, S. Li, Y. n. Chen, X. Li, and L. Yuan, "Identification and monitoring landslides in Longitudinal Range-Gorge Region with InSAR fusion integrated visibility analysis," *Landslides*, vol. 18, no. 2, pp. 551–568, 2020.

[16] X. Liu, C. Zhao, Q. Zhang et al., "Integration of Sentinel-1 and ALOS/PALSAR-2 SAR datasets for mapping active landslides along the Jinsha River corridor, China," *Engineering Geology*, vol. 284, p. 106033, 2021.

[17] Y. Zhang, X. Meng, G. Chen, L. Qiao, R. Zeng, and J. Chang, "Detection of geohazards in the Bailong River Basin using synthetic aperture radar interferometry," *Landslides*, vol. 13, no. 5, pp. 1273–1284, 2016.

[18] J. Dun, W. Feng, X. Yi, G. Zhang, and M. Wu, "Detection and mapping of active landslides before impound in the baihetan reservoir area (China) based on the time-series InSAR method," *Remote Sensing*, vol. 13, no. 16, p. 3213, 2021.

[19] A. C. Mondini, F. Guzzetti, K.-T. Chang, O. Monserrat, T. R. Martha, and A. Manconi, "Landslide failures detection and mapping using Synthetic Aperture Radar: past, present and future," *Earth-Science Reviews*, vol. 216, p. 103574, 2021.

[20] Z. Yang, Z. Li, J. Zhu, Y. Wang, and L. Wu, "Use of SAR/InSAR in mining deformation monitoring, parameter inversion, and forward predictions: a review," *IEEE Geoscience and Remote Sensing Magazine*, vol. 8, no. 1, pp. 71–90, 2020.

[21] E. Bayramov, M. Buchroithner, and M. Kada, "Radar remote sensing to supplement pipeline surveillance programs through measurements of surface deformations and identification of geohazard risks," *Remote Sensing*, vol. 12, no. 23, p. 3934, 2020.

[22] J. Galve, J. Pérez-Peña, J. Azañón et al., "Evaluation of the SBAS InSAR Service of the European space agency's geohazard exploitation platform (GEP)," *Remote Sensing*, vol. 9, no. 12, p. 1291, 2017.

[23] L. Li, X. Yao, J. Yao, Z. Zhou, X. Feng, and X. Liu, "Analysis of deformation characteristics for a reservoir landslide before and after impoundment by multiple D-InSAR observations at Jinshajiang River, China," *Natural Hazards*, vol. 98, no. 2, pp. 719–733, 2019.

[24] N. Richter and J.-L. Froger, "The role of interferometric synthetic aperture radar in detecting, mapping, monitoring, and modelling the volcanic activity of piton de la Fournaise, La réunion: a review," *Remote Sensing*, vol. 12, no. 6, p. 1019, 2020.

[25] L. Solari, M. Del Soldato, F. Raspini et al., "Review of satellite interferometry for landslide detection in Italy," *Remote Sensing*, vol. 12, no. 8, p. 1351, 2020.

[26] B. Osmanoğlu, F. Sunar, S. Wdowinski, and E. Cabral-Cano, "Time series analysis of InSAR data: methods and trends," *ISPRS Journal of Photogrammetry and Remote Sensing*, vol. 115, pp. 90–102, 2016.

[27] L. Zhang, K. Dai, J. Deng et al., "Identifying potential landslides by stacking-InSAR in southwestern China and its performance comparison with SBAS-InSAR," *Remote Sensing*, vol. 13, no. 18, p. 3662, 2021.

[28] J. Wasowski and F. Bovenga, "Investigating landslides and unstable slopes with satellite Multi Temporal Interferometry: current issues and future perspectives," *Engineering Geology*, vol. 174, pp. 103–138, 2014, https://doi.org/10.1016/j.enggeo.2014.03.003.

[29] P. Berardino, G. Fornaro, R. Lanari, and E. Sansosti, "A new algorithm for surface deformation monitoring based on small baseline differential SAR interferograms," *IEEE Transactions on Geoscience and Remote Sensing*, vol. 40, no. 11, pp. 2375–2383, 2002.

[30] S. Usai, "A least squares database approach for SAR interferometric data," *IEEE Transactions on Geoscience and Remote Sensing*, vol. 41, no. 4, pp. 753–760, 2003.

[31] R. Lanari, F. Casu, M. Manzo et al., "An overview of the small BAseline subset algorithm: a DInSAR technique for surface deformation analysis," *Pure and Applied Geophysics*, vol. 164, no. 4, pp. 637–661, 2007.

[32] A. Ferretti, C. Prati, and F. Rocca, "Nonlinear subsidence rate estimation using permanent scatterers in differential SAR interferometry," *IEEE Transactions on Geoscience and Remote Sensing*, vol. 38, no. 5, pp. 2202–2212, 2000.

[33] R. Lanari, O. Mora, M. Manunta, J. J. Mallorqui, P. Berardino, and E. Sansosti, "A small-baseline approach for investigating deformations on full-resolution differential SAR interferograms," *IEEE Transactions on Geoscience and Remote Sensing*, vol. 42, no. 7, pp. 1377–1386, 2004.

[34] X. Shi, L. Zhang, C. Zhou, M. Li, and M. Liao, "Retrieval of time series three-dimensional landslide surface displacements from multi-angular SAR observations," *Landslides*, vol. 15, no. 5, pp. 1015–1027, 2018.

[35] S. Samsonov, A. Dille, O. Dewitte, F. Kervyn, and N. D'Oreye, "Satellite interferometry for mapping surface deformation time series in one, two and three dimensions: a new method illustrated on a slow-moving landslide," *Engineering Geology*, vol. 266, p. 105471, 2020.

[36] C. Colesanti and J. Wasowski, "Investigating landslides with space-borne synthetic aperture radar (SAR) interferometry," *Engineering Geology*, vol. 88, no. 3-4, pp. 173–199, 2006.

[37] L. Cascini, G. Fornaro, and D. Peduto, "Advanced low- and full-resolution DInSAR map generation for slow-moving landslide analysis at different scales," *Engineering Geology*, vol. 112, no. 1-4, pp. 29–42, 2010.

[38] G. Herrera, F. Gutiérrez, J. C. García-Davalillo et al., "Multi-sensor advanced DInSAR monitoring of very slow landslides: the Tena Valley case study (Central Spanish Pyrenees)," *Remote Sensing of Environment*, vol. 128, pp. 31–43, 2013.

[39] O. Hungr, S. Leroueil, and L. Picarelli, "The Varnes classification of landslide types, an update," *Landslides*, vol. 11, no. 2, pp. 167–194, 2014.

[40] R. Schlögel, C. Doubre, J.-P. Malet, and F. Masson, "Landslide deformation monitoring with ALOS/PALSAR imagery: a D-InSAR geomorphological interpretation method," *Geomorphology*, vol. 231, pp. 314–330, 2015.

[41] R. Schlögel, J.-P. Malet, C. Doubre, and T. Lebourg, "Structural control on the kinematics of the deep-seated La Clapière landslide revealed by L-band InSAR observations," *Landslides*, vol. 13, no. 5, pp. 1005–1018, 2016.

[42] X. Yi, W. Feng, H. Bai, H. Shen, and H. Li, "Catastrophic landslide triggered by persistent rainfall in Sichuan, China: August 21, 2020, Zhonghaicun landslide," *Landslides*, vol. 18, no. 8, pp. 2907–2921, 2021.

[43] H. Bai, W. Feng, X. Yi et al., "Group-occurring landslides and debris flows caused by the continuous heavy rainfall in June 2019 in mibei village, longchuan county, guangdong province, China," *Natural Hazards*, vol. 108, no. 3, pp. 3181–3201, 2021.

[44] B. Bayer, A. Simoni, M. Mulas, A. Corsini, and D. Schmidt, "Deformation responses of slow moving landslides to seasonal rainfall in the Northern Apennines, measured by InSAR," *Geomorphology*, vol. 308, pp. 293–306, 2018.

[45] M. Saito, "Forecasting time of slope failure by tertiary creep," *Proceedings of the 7th International Conference on Soil Mechanics and Foundation Engineering*, vol. 2, pp. 677–683, 1969.

[46] N. Ju, J. Huang, C. He et al., "Landslide early warning, case studies from Southwest China," *Engineering Geology*, vol. 279, p. 105917, 2020.

[47] Q. Xu, Y. P. Zeng, J. P. Qian, C. J. Wang, and C. J. He, "Study on a improved tangential angle and the corresponding landslide pre-warning criteria," *Geological Bulletin of China*, vol. 28, pp. 501–505, 2009.

[48] Q. Xu, Y. Yuan, Y. Zeng, and R. Hack, "Some new pre-warning criteria for creep slope failure," *Science China Technological Sciences*, vol. 54, no. S1, pp. 210–220, 2011.

[49] X. Fan, Q. Xu, J. Liu et al., "Successful early warning and emergency response of a disastrous rockslide in Guizhou province, China," *Landslides*, vol. 16, no. 12, pp. 2445–2457, 2019.

[50] R. Huang, J. Huang, N. Ju, C. He, and W. Li, "WebGIS-based information management system for landslides triggered by Wenchuan earthquake," *Natural Hazards*, vol. 65, no. 3, pp. 1507–1517, 2013.

[51] Q. Xu, D. Peng, S. Zhang et al., "Successful implementations of a real-time and intelligent early warning system for loess landslides on the Heifangtai terrace, China," *Engineering Geology*, vol. 278, p. 105817, 2020.

[52] N.-p. Ju, J. Huang, R.-q. Huang, C.-y. He, and Y.-r. Li, "A Real-time monitoring and early warning system for landslides in Southwest China," *Journal of Mountain Science*, vol. 12, no. 5, pp. 1219–1228, 2015.

[53] J. Huang, R. Huang, N. Ju, Q. Xu, and C. He, "3D WebGIS-based platform for debris flow early warning: a case study," *Engineering Geology*, vol. 197, pp. 57–66, 2015.

[54] Z. Li, C. Song, and Y. Chen, "Application of satellite radar remote sensing to landslide detection and monitoring: challenges and solutions geomatics and," *Information Science of Wuhan University*, vol. 44, no. 7, pp. 967–979, 2019.

[55] F. Ji, C. Liu, Y. Shi, W. Feng, and D. Wang, "Characteristics and parameters of bank collapse in coarse-grained-material reservoirs based on back analysis and long sequence monitoring," *Geomorphology*, vol. 333, pp. 92–104, 2019.